Anomalous structural phase transformation in swift heavy ion-irradiated δ-Sc4Hf3O12

Masanari Iwasaki, Yusuke Kanazawa, Daiki Manago, Maulik Patel, Gianguido Baldinozzi, Kurt E. Sickafus, Manabu Ishimaru

▶ **To cite this version:**

Masanari Iwasaki, Yusuke Kanazawa, Daiki Manago, Maulik Patel, Gianguido Baldinozzi, et al.. Anomalous structural phase transformation in swift heavy ion-irradiated δ-Sc4Hf3O12. Journal of Applied Physics, 2022, 132, pp.075901. 10.1063/5.0098518 . hal-03744856

HAL Id: hal-03744856
https://hal.science/hal-03744856

Submitted on 3 Aug 2022

HAL is a multi-disciplinary open access archive for the deposit and dissemination of scientific research documents, whether they are published or not. The documents may come from teaching and research institutions in France or abroad, or from public or private research centers.

L'archive ouverte pluridisciplinaire **HAL**, est destinée au dépôt et à la diffusion de documents scientifiques de niveau recherche, publiés ou non, émanant des établissements d'enseignement et de recherche français ou étrangers, des laboratoires publics ou privés.

Anomalous structural phase transformation in swift heavy ion-irradiated δ-$Sc_4Hf_3O_{12}$

Masanari Iwasaki,[1] Yusuke Kanazawa,[1] Daiki Manago,[1] Maulik K. Patel,[2] Gianguido Baldinozzi,[3] and Kurt E. Sickafus,[4] and Manabu Ishimaru[1,*]

[1]*Department of Materials Science and Engineering, Kyushu Institute of Technology, Fukuoka 804-8550, Japan*

[2]*Department of Mechanical, Materials, and Aerospace Engineering, The University of Liverpool, Liverpool L69 3GH, United Kingdom*

[3]*Structures, Propriétés et Modélisation des Solides, Université Paris-Saclay, CentraleSupelec, CNRS, 91190 Gif-sur-Yvette, France*

[4]*Materials Science and Technology Division, Los Alamos National Laboratory, Los Alamos, NM 87545, USA*

Abstract

Swift heavy ion irradiation was carried out to examine the ionization effects on structural changes of δ-$Sc_4Hf_3O_{12}$ in which oxygen vacancies are regularly arranged. The specimens were irradiated at room temperature with 92 MeV xenon ions to fluences ranging from 3×10^{12} to 1×10^{14} /cm^2, and characterized by grazing (glancing) incidence x-ray diffraction, transmission electron microscopy, and scanning transmission electron microscopy. It was found that the pristine long-range ordered rhombohedral δ-phase undergoes a reconstructive transformation towards a long-range disordered cubic oxygen-deficient fluorite phase promoted by ionization effects. In addition, an ordered phase with a short-range structure different from the δ-type was formed in a layer going from the surface to a depth of ~4.5 μm in the specimen irradiated to a fluence of 1×10^{14} /cm^2. It was found that the ordered phase is formed from the disordered cubic fluorite phase. This structural change is anomalous, because it is the opposite process of the usual irradiation-induced structural change, the order-to-disorder phase transformation. Electron diffraction experiments revealed that short-range ordered regions in this layer possess an oxygen-excess bixbyite organization (*C*-type heavy rare-earth oxides) with randomly filled anion vacant sites to account for the different stoichiometry, and a long-range average oxygen-

deficient fluorite phase.

*Corresponding author: ishimaru@post.matsc.kyutech.ac.jp

1. Introduction

Ceramic materials play an important role in various industries as structural and functional materials due to their excellent mechanical properties, unique physical characteristics, and chemical durability. In the nuclear industry, ceramics are currently used as the nuclear fuels, fission reaction control materials, and neutron shielding materials. The structural materials of nuclear power plants and fusion reactors are often exposed to harsh radiation environments. In addition, ceramic materials are candidate system for encapsulating minor actinides or toy models for parametric studies of advanced fuels. The fabrication and performance of advanced nuclear fuels, particularly those containing the minor actinides, is an important challenge that requires a fundamental understanding of the structural behavior of complex materials during processing and irradiation. Creating novel tailored fuel forms requires appropriate experimental efforts to outline the specific features of the radiation-induced changes in model systems, an essential step for feeding high-throughput *ab initio* calculations of materials properties.

Oxide ceramics with a fluorite-type structure, where metal cations form a face-centered cubic lattice and oxygen anions occupy its tetrahedral interstitial sites, are known to exhibit excellent radiation resistance [1-4], as already seen in uranium dioxide and zirconium dioxide. Oxygen-deficient fluorite structural derivatives ($M_{1-x}M'_xO_{2-x}$, where M and M' are aliovalent metal cations and O is the anion), which contain oxygen vacancies to provide a charge compensation mechanism that satisfies the electroneutrality, have also attracted attention for their radiation effects, because of their structural similarity to fluorite. There are variety of oxygen-deficient fluorite structural derivatives, such as pyrochlore [5-8], murataite [9], bixbyite [10,11], and δ-phase compounds [12,13]; some of them are highly resistant to radiation-induced amorphization.

The degradation of materials under radiation environments is induced by two effects: knock-on binary collision effects and ionization one. These effects lead to an order-disorder transformation to defect-fluorite [6,8-13] and amorphization [6-9]. We have previously investigated the structural changes of δ-$Sc_4Zr_3O_{12}$ under 300 keV krypton ion irradiations in which knock-on effects are pronounced [14]. As already

reported in literature for other oxygen-deficient fluorite structural derivatives, long-range reconstructive transformations were observed for the ordered δ-rhombohedral to disordered oxygen-deficient cubic fluorite phase, which is consistent with the scandia-zirconia pseudo-binary phase diagram [15,16]. In addition, the formation of a metastable phase with a bixbyite (*C*-rare-earth) structure was confirmed [14]. Irradiations generally induce an order-to-disorder phase transformation, and the phase observed after irradiation is sometimes known as a high temperature or pressure polymorph. Because of this viewpoint, the formation of ordered oxygen-excess bixbyite regions within a long-range disordered oxygen-deficient fluorite phase is anomalous. On the other hand, no bixbyite phase was observed in 185 MeV gold ion irradiated δ-$Sc_4Zr_3O_{12}$ in which ionization effects are dominant [17]. The pseudo-binary scandia-hafnia system [18] contains several ordered compounds, where the structural motifs consist of similar coordination polyhedra. These compounds are known as β-, γ-, and δ-type phases, with composition limits equivalent to the scandia-zirconia ones [15,16]. Using quantitative x-ray diffraction analysis, we had recently shown that δ-$Sc_4Hf_3O_{12}$ transforms to a long-range oxygen-deficient defect fluorite structure with indications of short-range nano-scale regions of local oxygen-excess bixbyite organization [19]. In the present work, we extend our current understanding with a detailed electron microscopy analysis of swift heavy ion irradiated δ-$Sc_4Hf_3O_{12}$, and examine the structural changes induced by ionization effects.

2. Experimental

$Sc_4Hf_3O_{12}$ samples were made using standard solid state synthesis by mixing scandium sesquioxide (Sc_2O_3, 99.99%) and hafnium dioxide (HfO_2, 99.95%) powders (Alfa Aesar, A Johnson Matthey Company) in stoichiometric amounts. Powders were calcined before mixing them in a high-energy ball mill (SPEX 8000D dual mixer/mill) using a zirconia ceramic vial set and two zirconia ceramic balls in an isopropanol medium for 8 hours. 13 mm diameter pellets were made in an iso-static press using a stainless steel die and plunger. The pellets were then sintered in air, first at 1200 ºC for 48 hours and then again at 1600 ºC for 72 hours. The

heating and cooling rates during both sintering cycles were kept at 5 °C/min. Samples were ground again between the two sintering cycles. The as-synthesized pellets were approximately 95% of the theoretical maximum density. The sintered pellets were then cut and polished using diamond saw and diamond lapping films down to 1 μm and a final polish using colloidal silica.

The sintered pellets were irradiated at room temperature with 92 MeV xenon (Xe^{26+}) ions to fluences ranging from 3×10^{12} to 1×10^{14} /cm^2 using IRRSUD beamline at GANIL (The Grand Accélérateur National d'Ions Lourds) in Caen, France. SRIM (The Stopping and Range of Ions in Matter [20]) calculations showed that these ions deposit energy predominantly in the electronic stopping regime with ~15-20 keV/nm/ion within the first 4 μm of depth and a total projected range of ~8 μm. Detailed SRIM plots can be found in Ref. 19. The ion irradiated specimens were characterized by grazing (glancing) incidence x-ray diffraction (GIXRD), transmission electron microscopy (TEM), and scanning transmission electron microscopy (STEM). GIXRD measurements were carried out on a Rigaku SmartLab x-ray diffractometer using Cu-K_α radiation at 40 kV and 200 mA, and the incident angle of x-rays was set to ω=1° and 5°. Cross-sectional and plan-view TEM/STEM specimens were prepared by the mechanical polishing in combination with Ar ion milling or focused ion beam fabrications. The TEM samples were carbon coated to avoid charge-up during observations. The specimens were examined by TEM using JEOL JEM-3000F and F200 operated at an acceleration voltage of 300 kV and 200 kV, respectively.

3. Results

Figure 1 shows the GIXRD profiles obtained from pristine and ion irradiated δ-$Sc_4Hf_3O_{12}$; the incident angles of x-rays was set to (a) 1° and (b) 5°. To enhance weak reflections, the vertical axis is plotted in logarithmic scale. The penetration depth of Cu-K_α x-rays, t, corresponding to 99% of the scattered intensity of the x-ray beam, is expressed by the following equation [21]:

$$t = \frac{4.61}{\mu} / \left(\frac{1}{\sin\omega} + \frac{1}{\sin(2\theta - \omega)}\right),$$

where ω and 2θ are the incidence and scattering angle of the x-rays, respectively, and μ is the linear attenuation coefficient of the sample. Based on this formula, the penetration depth of x-rays was estimated to ~0.9 μm at an incident angle of 1° and ~4.1 μm at 5°. In addition to the fundamental lattice reflections, superlattice reflections due to the ordering of oxygen vacancies can be clearly observed in the pristine specimen. The peak position is consistent with that of a rhombohedral δ-type structure [18,19,22] shown on the abscissa of Fig. 1(b). For the specimen irradiated to a fluence of 1×10^{13} cm^{-2}, the GIXRD profile is almost the same regardless of the incident angle of x-rays. In the specimen irradiated to 3×10^{13} cm^{-2}, the superlattice reflections are clearly visible in the GIXRD profile at 5°, whereas some of them disappear in the 3° profile. This suggests that the structural changes are remarkable just beneath the surface. Finally, the superlattice reflections disappear at 1×10^{14} cm^{-2}, indicating the occurrence of an order-to-disorder phase transformation. In our previous study, we had observed the emergence of a broad peak around 22° in 2θ which was attributed to a possible *C*-type oxygen-excess bixbyite type phase [19]. This broad peak is also observed in the GIXRD patterns shown in Figs. 1(a) and 1(b).

As described above, the impinging ions penetrate up to a depth of about 8 μm below the surface according to the present irradiation conditions [19]. To examine the structural evolution of δ-$Sc_4Hf_3O_{12}$ under swift heavy ion irradiation, cross-sectional TEM observations were performed. Figure 2 shows cross-sectional bright-field TEM images of the specimens irradiated to ion fluences of (a) 1×10^{13}, (b) 3×10^{13}, and (c) 1×10^{14} cm^{-2}. For comparison, electronic (S_e) and nuclear stopping powers (S_n) and their ratio (S_e/S_n) are also shown in Fig. 2(d). No significant features except for the diffraction contrast caused by the polycrystals are detected in Fig. 2(a), whereas a damage layer is formed in Fig. 2(b). It should be noted that the picture contrast abruptly changes at ~4.5 μm, indicated by the line in Fig. 2(c). This suggests that the significant structural changes occur beneath the surface of δ-$Sc_4Hf_3O_{12}$ spanning a depth of several micrometers. It was confirmed that the crystallinity is still maintained at the highest fluence and no amorphization occurs. Structural changes under the irradiation environments are induced by two effects: knock-on effect and ionization one. Under the present

irradiation conditions, the S_e is ~10 keV/nm/ion at 4.5 μm (Fig. 2(d)), which is ~20 times larger than the S_n: the structural changes at the surface observed here are mainly induced by ionization effects.

To identify the origin of the contrast change at ~4.5 μm in the specimen irradiated to a fluence of 1×10^{14} /cm^2, electron diffraction experiments were performed. Figure 3 shows the selected-area electron diffraction patterns taken from (a) just above and (b) just below the contrast interface described in Fig. 2(c). These patterns were obtained from the same crystal grain using an electron beam of ~200 nm in diameter, as shown in Fig. 2(c). The superlattice reflections due to the ordering of the oxygen vacancies disappear in Fig. 3(b). In contrast, superlattice reflections are observed in Fig. 3(a), but their positions do not agree with those of the δ-type structure. To determine the crystal structure, the structure factors for the *hkl* reflection, F_{hkl}, were calculated on the basis of the kinematical approximation: $F_{hkl} = \sum_j^n f_j e^{-2\pi i(hx_j+ky_j+lz_j)}$, where f_j is atomic scattering factor of *j*-th atom, and x_j, y_j, z_j are the atomic position of *j*-th atom. It was found that the diffraction pattern of Fig. 3(b) corresponds to the (011) reciprocal lattice plane of the fluorite structure (Fig. 3(b')). This suggests the mesoscale structural organization changes from ordered δ to disorder fluorite. From the diffraction patterns of Fig. 3(a) and others in different crystallographic orientations (see below), the formation of the oxygen-excess bixbyite (*C*-rare-earth) phase was confirmed at the region from the surface to a depth of 4.5 μm. (The structure factors of the ideal bixbyite structure can be found elsewhere [14].) For example, the diffraction pattern of Fig. 3(a) corresponds to that of the bixbyite structure viewed along the [011] direction (Fig. 3(a')). Note that the 011- and 033-type reflections appear in the experimental diffraction pattern due to double diffraction, as described below. The following crystallographic orientation relationships exist between the fluorite and bixbyite phases: $(100)_B$ // $(100)_F$ and $[011]_B$ // $[011]_F$, where 'B' and 'F' denote the bixbyite and fluorite lattices, respectively.

Figure 4(a) shows a magnified bright-field image where the contrast interface at ~4.5 μm is clearly visible. To examine the distribution of the bixbyite phase, dark-field TEM observations were performed. The dark-field image of Fig. 4(b) was taken by using the fundamental lattice spot. The whole area reveals the bright

contrast, indicating that this region is a single crystal. On the other hand, there are bright dots at just above the interface in the dark-field image of Fig. 4(c) which was taken using the superlattice reflection due to the bixbyite phase. This suggests that these are correlated to bixbyite clusters (variants) with a size of <10 nm embedded in their average fluorite matrix. It should be noted that each dot has a different brightness, which is presumably due to the statistical fluctuations in their spatial correlation. Because of their small spatial correlation length, the Bragg reflections produced by this bixbyite-type phase are weak and broad; therefore, their reflections are not sharp in the GIXRD profiles and contribute to the diffuse scattering of Fig. 1. The diffuse scattering takes the form of broad features that exist around 2θ=18-25° and 40-50° in the GIXRD profile of the specimen irradiated to 1×10^{14} /cm^2 [19].

4. Discussion

The formation of the bixbyite phase was previously observed in δ-$Sc_4Zr_3O_{12}$ irradiated at cryogenic temperature with 300 keV Kr ions to a fluence of 3×10^{16} /cm^2 [14]. The damage was equivalent to a peak dose of ~70 displacements per target atom: the knock-on effect plays an important role for the formation of the bixbyite phase. On the other hand, the present study clearly reveals that the bixbyite phase is also formed by ionization effects in the supposedly iso-structural δ-$Sc_4Hf_3O_{12}$. A clear interface between the fluorite matrix with and without the bixbyite clusters is located at ~4.5 μm from the surface where the electronic stopping power is ~10 kV/nm/ion. This suggests that there is a critical electronic stopping power for the formation of the bixbyite phase. As seen by many researchers in the past that ions with different electronic stopping power does create different ion track sizes, with the track being defined by the extent of quenching from a thermal spike surpassing the melting temperature of the material. In the present case while this might be the case it will take further ion irradiation studies to determine ions with varying electronic stopping to quantify the threshold in S_e for which these modifications occur.

There is a crystallographic orientation relationship between the bixbyite and fluorite phases, as

described above, suggesting that the disordered fluorite phase is formed by ensemble averages of the bixbyite variants. This means the following structural changes were induced by irradiation: δ-type (space group: $R\bar{3}$ (No. 148)) → fluorite ($Fm\bar{3}m$ (No. 225)) → bixbyite ($Ia\bar{3}$ (No. 206)). The formation of oxygen-excess bixbyite can be explained by a reconstructive mechanism. While most of the radiation-induced structural changes are from the low-temperature ordered phase to the high-temperature and higher symmetry phase of the phase diagram, there is absolutely no requirement for that as any other transformation to another phase increasing the overall entropy of the system can be favored.

It is interesting to see how a single ion in swift heavy ion irradiation leads to structural changes of δ-$Sc_4Zr_3O_{12}$. Figure 5 shows a plan-view high-resolution TEM image of the specimen irradiated to a fluence of 3×10^{12} /cm^2. Since the plan-view TEM sample was prepared by a combination of mechanical polishing and ion milling, the depth at which this image was obtained from the surface is unknown. The electron beam is incident along the [111] direction of $Sc_4Zr_3O_{12}$, and the lattice fringes with ~0.6 nm interval correspond to the superlattice due to oxygen vacancy ordering. An ion track with a diameter of ~3 nm is present at the central region of the image. The lattice fringes become weak or disappear at the ion track, suggesting that the ordered δ-phase transforms to the disordered phase by a single swift heavy ion. This result is consistent with the transformation from the ordered δ to disordered fluorite phase.

The space group $R\bar{3}$ is a subgroup of both $Fm\bar{3}m$ and $Ia\bar{3}$, and the symmetry of $Ia\bar{3}$ is also a subgroup of the disordered parent structure ($Fm\bar{3}m$). A reconstructive mechanism between the δ and the bixbyite phase is then perfectly possible from a theoretical point of view and it involves the $Fm\bar{3}m$ phase. Recently, the actual $Ia\bar{3}$ symmetry of the oxygen-excess bixbyite was questioned proposing a subgroup where the oxygen vacancies of the compound $Gd_2Ce_2O_7$ can order. The different stoichiometry of the δ phase under investigation is not favorable for a same ordering mechanism that requires a long-range fluctuation of oxygen stoichiometry. In $Gd_2Ce_2O_7$, half of the vacancy sites of the ideal bixbyite anionic sublattice are filled, and this structure is called the ordered 'anion-excess bixbyite' [11]. This structure has space group $I2_13$ (No. 199), which also has a group and subgroup

relationship with $Fm\bar{3}m$. The ideal and anion-excess bixbyite phases can be distinguished by examining the extinction rule of the structure factor. Figures 6(a) and 6(b) show the selected-area electron diffraction patterns, respectively, viewed along the [100] and [111] directions of the bixbyite structure. The corresponding simulated diffraction patterns of the ideal and anion-excess bixbyite structure are also shown in Figs. 6(a', b') and 6(a'', b''), respectively. The $Ia\bar{3}$ and $I2_13$ symmetry can be distinguished by examining the extinction rule of 0*kl*-type reflections: they disappear in the ideal bixbyite structure when *k* and *l* are odd (circled in Fig. 6(b')), while all reflections are allowed in the anion-excess bixbyite one (the intensity of the 022-type reflections are very weak). Although 011- and 033-type reflections exist in the (111) diffraction pattern (Fig. 6(b)), they are not present in the (100) diffraction pattern (Fig. 6(a)). This means that the 011 and 033 reflections are forbidden, but they accidentally appear due to double diffraction. This suggests that the ion-beam-induced phase possesses the average bixbyite structures ($Ia\bar{3}$) where the excess oxygen atoms are distributed to fill randomly a fraction of the vacant sites of the ideal bixbyite structure, a result that provides a large entropic contribution for the stabilization of this phase.

We have previously performed compositional analyses of 300 keV Kr ion irradiated δ-$Sc_4Zr_3O_{12}$ using energy-dispersive x-ray spectroscopy (EDX), Rutherford backscattering spectroscopy, and x-ray photoelectron spectroscopy [23]. As a result, it was found that the composition of the irradiation-induced phases, i.e., fluorite and bixbyite, is almost the same as that of the pristine δ-type phase (60 at.%ZrO_2 for $Sc_4Zr_3O_{12}$). This composition is quite different from that of the bixbyite phase (~24 at.%ZrO_2) present in the Sc_2O_3-ZrO_2 pseudo-binary phase diagram. To confirm the compositional change of swift heavy ion irradiated δ-$Sc_4Hf_3O_{12}$, we performed elemental mapping by using EDX. Figure 7(a) shows the annular bright-field image taken from the interface between the bixbyite (left) and fluorite (right) regions. The corresponding elemental maps taken by the characteristic x-rays of (b) Sc-*K*, (c) Hf-*M*, and (d) O-*K* reveal the distribution of the elements is almost uniform, suggesting that no remarkable compositional change of the cation sublattice takes place at the fluorite to bixbyite phase transformation. Although the phase diagram of the Sc_2O_3-HfO_2 system is not well established yet, the solubility limit of HfO_2 in a Sc_2O_3 bixbyite phase is 16-24 at.% [15]. It

is thought that this discrepancy between the present experimental results and the composition predicted from the phase diagram can be explained by considering size effects responsible for an interface energy contribution to the free energy for the nanocrystalline material. It has been reported that the solubility limit in solid solution or intermetallic compounds is significantly increased in nanometer-sized alloy systems [24-28]. For example, Ge nanocrystallites contain ~30 at.%Sn which is much larger than the solubility limit of Sn in *bulk* Ge crystal (~1 at.%) [29-31]. The size of the bixbyite phase induced by irradiation is less than 10 nm, as shown in Fig. 4(c) and our previous study [14]. Because of this, there is a possibility that the bixbyite phase may contain more Hf than the solid solution limit predicted from the *bulk* phase diagram.

5. Conclusions

Thus, to conclude, detailed TEM investigation shows that δ-$Sc_4Hf_3O_{12}$ transforms to a defect fluorite but with mescoscopic correlations characteristic of a bixbyite phase with a topotactic relationship to the parent fluorite structure. The ordered oxygen-excess bixbyite phase exists as nanoscale regions only in a layer of about 4.5 μm beneath the sample surface, suggesting that there is a threshold in the electronic stopping which may be required to quench this phase. These results complement our previous work on swift heavy ion irradiations of δ-$Sc_4Hf_3O_{12}$ and $Gd_2Ce_2O_7$ and provide strong basis to the fact that disordering processes in fluorite related systems are more complex than initially thought and, that the local motifs that build the structure in disordered oxides can be arranged in a way significantly different from the statistical description of the average structure.

Acknowledgements

This work was supported in part by Grant-in-Aid for Scientific Research (B) (Grant No. 19H02463) from the Ministry of Education, Sports, Science, and Technology, Japan (MI). This work was also supported by JKA and its promotion funds from KEIRIN RACE (MI). A part of this work was supported by "Advanced Characterization Nanotechnology Platform, Nanotechnology Platform Program of the Ministry of Education,

Culture, Sports, Science and Technology (MEXT), Japan" at the Ultramicroscopy Research Center in Kyushu University (A-21-KU-0411). We are grateful to Dr. Mitsunari Auchi of Kyushu University for his helpful support in focused ion beam fabrications. The GIXRD measurements and EDX elemental mapping were supported by Mr. Katsumi Yamamoto and Mr. Noboru Wakayama of the Center for Instrumental Analysis, Kyushu Institute of Technology. We would like to thank Dr. Clara Grygiel of the GANIL and CIMAP for assistance and support in using beamline IRRSUD.

Conflict of Interest

The authors have no conflicts to disclose.

DATA AVAILABILITY

The data that support the findings of this study are available from the corresponding author upon reasonable request.

References

[1] Hj. Matzke and J. L. Whitton, Can. J. Phys. **44**, 995 (1966).

[2] K. E. Sickafus, Hj. Matzke, Th. Hartmann, K. Yasuda, J. A. Valdez, P. Chodak III, M. Nastasi, and R. A. Verrall, J. Nucl. Mater. **274**, 66 (1999).

[3] T. Sonoda, M. Kinoshita, Y. Chimi, N. Ishikawa, M. Sakata, and A. Iwase, Nucl. Instrum. Meth. Phys. Res. B **250**, 254 (2006).

[4] C. Sabathier, L. Vincent, P. Garcia, F. Garrido, G. Carlot, L. Thome, P. Martina, C. Valot, Nucl. Instrum. Meth. Phys. Res. B **266**, 3027 (2008).

[5] S. X. Wang, B. D. Begg, L. M. Wang, R. C. Ewing, W. J. Weber, and K. V. G. Kutty, J. Mater. Res. **14**, 4470 (1999).

[6] K. E. Sickafus, L. Minervini, R. W. Grimes, J. A. Valdez, M. Ishimaru, F. Li, K. J. McClellan, and T. E. Hartmann, Science **289**, 748 (2000).

[7] J. Lian, X. T. Zu, K. V. G. Kutty, J. Chen, L. M. Wang, and R. C. Ewing, Phys. Rev. B **66**, 054108 (2002).

[8] G. Sattonnay, S. Moll, L. Thomé, C. Decorse, C. Legros, P. Simon, J. Jagielski, I. Jozwik, and I. Monnet, J. Appl. Phys. **108**, 103512 (2010).

[9] J. Lian, L. M. Wang, and R. C. Ewing, J. Appl. Phys. **97**, 113536 (2005).

[10] M. Tang, P. Lu, J. A. Valdez, and K.E. Sickafus, J. Appl. Phys. **99**, 063514 (2006).

[11] M. Patel, J. Aguiar, K. E. Sickafus, and G. Baldinozzi, Phys. Rev. Mater. **6**, 013610 (2022).

[12] K. E. Sickafus, R. W. Grimes, J. A. Valdez, A. Cleave, M. Tang, M. Ishimaru, S. M. Corish, C. R. Stanek, and B. P. Uberuaga, Nature Mater. **6**, 217 (2007).

[13] J. A. Valdez, M. Tang, and K. E. Sickafus, Nucl. Instrum. Meth. Phys. Res. B **250**, 148 (2006).

[14] M. Ishimaru, Y. Hirotsu, M. Tang, J. A. Valdez, and K. E. Sickafus, J. Appl. Phys. **102**, 063532 (2007).

[15] R. Ruh, H. J. Garrett, R. F. Domagala, and V. A. Patel, J. Am. Ceram. Soc. **60**, 399 (1977).

[16] H. M. Ondik and H. F. McMurdie, Phase Diagrams for Zirconium and Zirconia Systems (American Ceramic Society, Columbus, 1998).

[17] M. Tang, P. Kluth, J. Zhang, M. K. Patel, B. P. Uberuaga, C. J. Olson Reichhardt, and K. E. Sickafus, Nucl. Instrum. Meth. Phys. Res. B **268**, 3243 (2010).

[18] G. A. Kalinovskaya, F. M. Spiridonov, and L. X. Komissarova, J. Less-Common Met. **17**, 151 (1969).

[19] M. K. Patel, K. E. Sickafus, and G. Baldinozzi, Phys. Rev. Mater. **4**, 093605 (2020).

[20] J. F. Ziegler, J. P. Biersack, and U. Littmark, The Stopping and Range of Ions in Solids (Pergamon, New York, 1985).

[21] B. D. Cullity, Elements of X-ray diffraction, 2nd Ed. (Addison-Wesley Publishing Company Inc., 1978).

[22] H. J. Rossell, J. Solid State Chem. **19**, 103 (1976).

[23] K. E. Sickafus, M. Ishimaru, Y. Hirotsu, I. O. Usov, J. A. Valdez, P. Hosemann, A. L. Johnson, T. T. Thao, Nucl. Instrum. Meth. Phys. Res. B **266**, 2892 (2008).

[24] H. Yasuda and H. Mori, Phys. Rev. Lett. **69**, 3747 (1992).

[25] H. Yasuda and H. Mori, Z. Phys. D **31**, 131 (1994).

[26] H. Yasuda and H. Mori, J. Cryst. Growth **237-239**, 234 (2002).

[27] K. Kusada, H. Kobayashi, R. Ikeda, Y. Kubota, M. Takata, S. Toh, T. Yamamoto, S. Matsumura, N. Sumi, K. Sato, K. Nagaoka, and H. Kitagawa, J. Am. Chem. Soc., **136**, 1864 (2014).

[28] K. Kusada, D. Wu, Y. Nanba, M. Koyama, T. Yamamoto, X. Q. Tran, T. Toriyama, S. Matsumura, A. Ito, K. Sato, K. Nagaoka, O. Seo, C. Song, Y. Chen, N. Palina, L. S. R. Kumara, S. Hiroi, O. Sakata, S. Kawaguchi, Y. Kubota, and H. Kitagawa, Adv. Mater. **33**, 2005206 (2021).

[29] T. Kimura, M. Ishimaru, M. Okugawa, R. Nakamura, and H. Yasuda, Jpn. J. Appl. Phys. **56**, 100307 (2017).

[30] M. Higashiyama, M. Ishimaru, M. Okugawa, and R. Nakamura, J. Appl. Phys. **125**, 175703 (2019).

[31] K. Inenaga, R. Motomura, M. Ishimaru, R. Nakamura, and H. Yasuda, J. Appl. Phys. **127**, 205304 (2020).

Figure captions

Figure 1. GIXRD profiles of pristine and 92 MeV Xe ion irradiated δ-$Sc_4Hf_3O_{12}$ as a function of ion fluences. The incident angle of x-rays was fixed to (a) 1° and (b) 5°. The vertical axis is plotted on a logarithmic scale. For comparison, the peak positions of the δ-type structure are indicated by lines at the bottom of (b). Weak superlattice reflections due to the ordering of oxygen vacancies are observed at fluences up to 3×10^{13} cm^{-2}. On the other hand, they disappear in 1×10^{14} cm^{-2} irradiated specimens, suggesting that the ordered rhombohedral δ-phase is transformed into the disordered cubic fluorite phase. Double-headed arrows in (b) indicate the broad peaks distributed around 2θ=18-25° and 40-50°.

Figure 2. Cross-sectional bright-field TEM images of δ-$Sc_4Hf_3O_{12}$ irradiated to fluences of (a) 1×10^{13}, (b) 3×10^{13}, and (c) 1×10^{14} /cm^2. (d) Depth dependence of the electronic (S_e) and nuclear stopping powers (S_n) and their ratio (S_e/S_n) calculated by SRIM-2008. The scale of the TEM image is the same as the horizontal axis of the graph. Irradiation-induced damage is formed near the surface where electronic stopping power is much larger than nuclear stopping one. In addition to the diffraction contrast caused by polycrystals, the contrast changes abruptly at a depth of ~4.5 μm from the surface in (c). Bixbyite and fluorite phases are formed in regions shallower and deeper than the interface, respectively.

Figure 3. (a,b) Selected-area electron diffraction patterns of the specimen irradiated to a fluence of 1×10^{14} /cm^2. The patterns were taken from the region of (a) <4.5 μm and (b) >4.5 μm from the surface indicated by the circles in Fig. 2(c). Only fundamental lattice reflections are present in (b), whereas superlattice reflections appear in (a). Calculated diffraction patterns of (a') the bixbyite and (b') fluorite structures viewed along the [011] direction. The 0*kl*-type reflections with odd numbers of *k* and *l*, e.g., 011 and 033, for the bixbyite structure are forbidden reflections and appear by double diffraction in the experimental diffraction pattern of (a).

Figure 4. (a) Magnified bright-field TEM image taken from the interface between the bixbyite phase (left) and fluorite phase (right) regions. Dark-field TEM images taken by using (b) the fundamental lattice spot and (c) the superlattice spot due to bixbyite structure. The entire area exhibits bright contrast in (b), indicating that the region is a single crystal grain. In the region to the left of the interface in (c), the bixbyite clusters are densely dispersed.

Figure 5. Plan-view high-resolution TEM image viewed along the [111] direction of δ-$Sc_4Hf_3O_{12}$ irradiated to a fluence of 3×10^{12} /cm^2. The lattice fringes with an interval of ~0.6 nm correspond to the superlattice due to the oxygen vacancy ordering, which disappear at the ion track region.

Figure 6. Selected-area electron diffraction patterns of the bixbyite phase viewed along (a) the [100] and (b) [111] directions. Calculated diffraction patterns of (a', b') the ideal and (a'', b'') anion-excess bixbyite structures. The 0*kl*-type reflections with odd numbers of *k* and *l*, e.g., 011 and 033 (circled in (a') and (b')), observed in (b) do not exist in (a), indicating they appear in (b) due to double diffraction.

Figure 7. (a) Annular bright-field image and (b-d) elemental maps. (b) Sc-*K*, (c) Hf-*M*, and (d) O-*K*. 'B' and 'F' in (a) denote the region of the bixbyite and fluorite phase, respectively. There is no significant compositional difference in the whole area, suggesting that the composition of the bixbyite phase is almost the same as that of the fluorite phase.

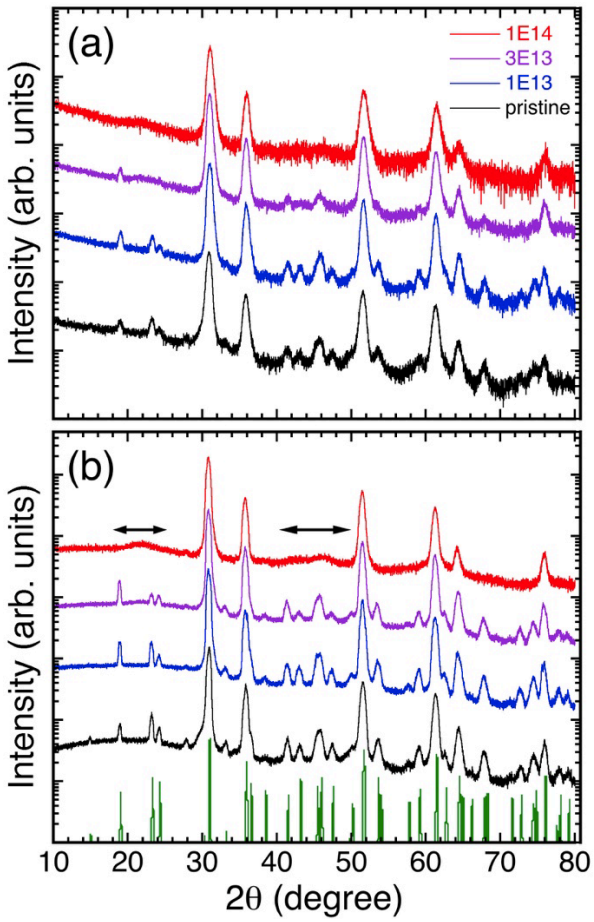
(a)
1E14
3E13
1E13
pristine
Intensity (arb. units)
(b)
Intensity (arb. units)
10
20
30
40
50
60
70
80
2θ (degree)

FIG. 1

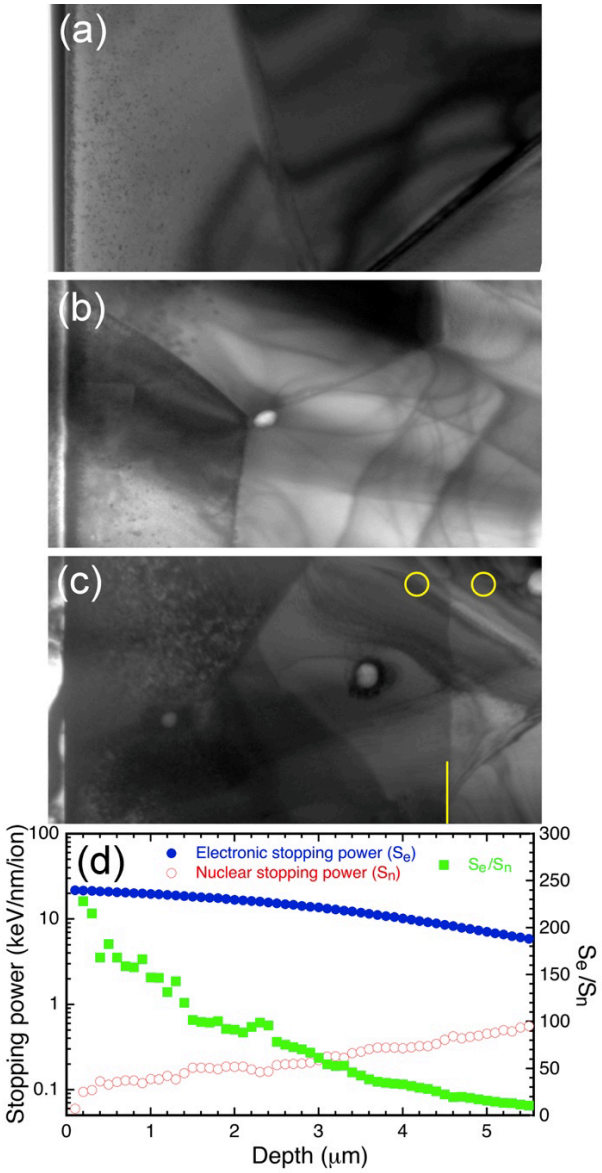
(a)
(b)
(c)
(d)
Electronic stopping power (S_e)
Nuclear stopping power (S_n)
S_e/S_n
Stopping power (keV/nm/ion)
S_e/S_n
Depth (μm)
100
10
1
0.1
300
250
200
150
100
50
0
0
1
2
3
4
5

FIG. 2

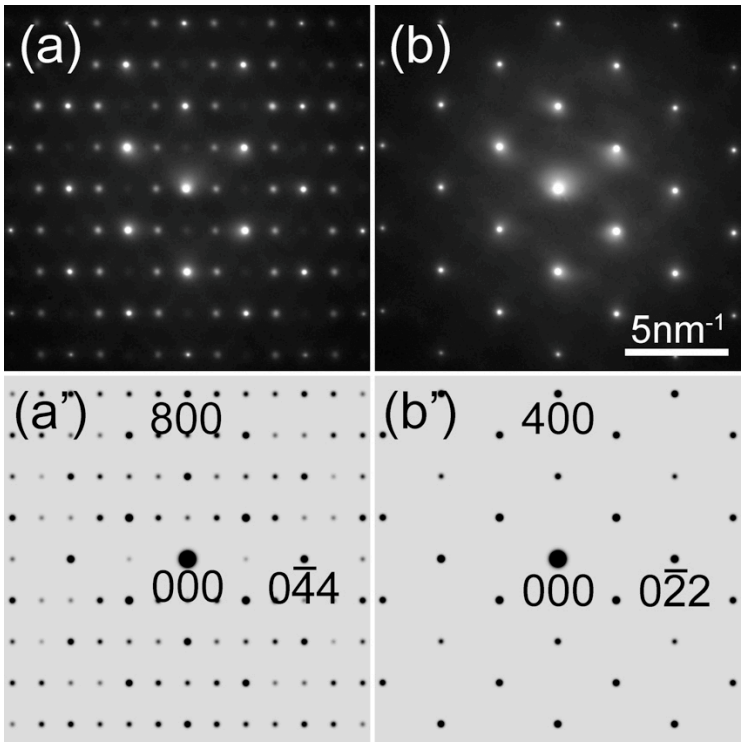

FIG. 3

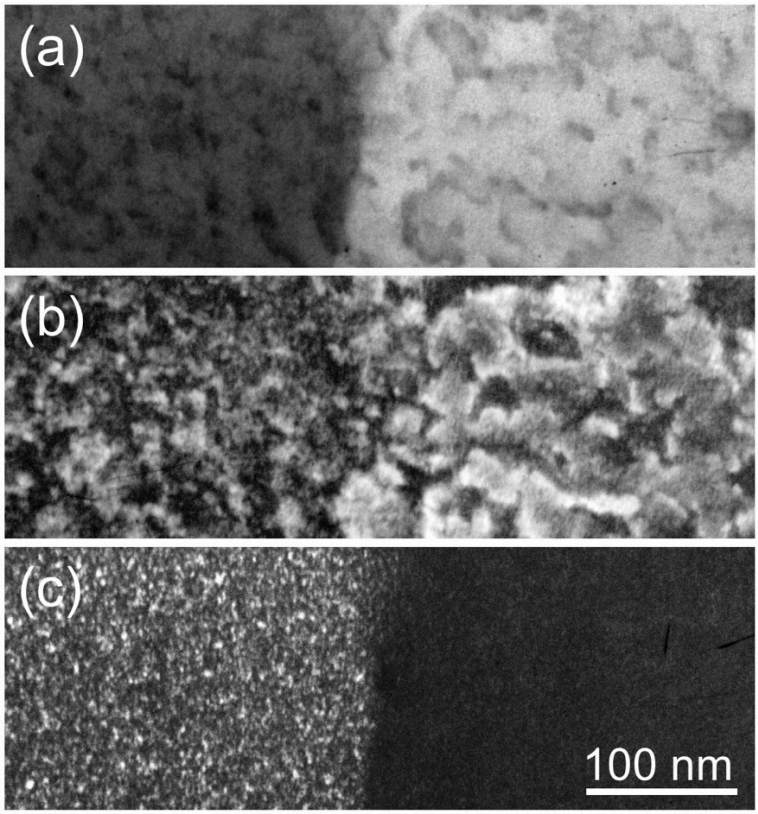

FIG. 4

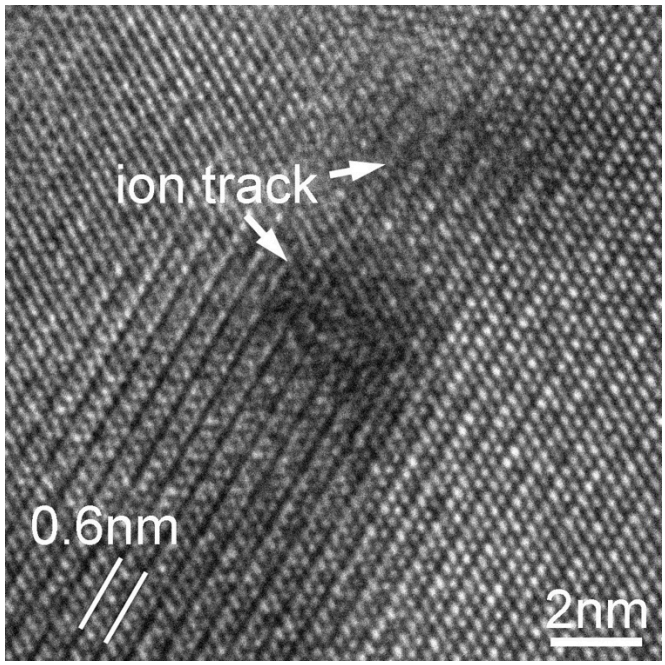

FIG. 5

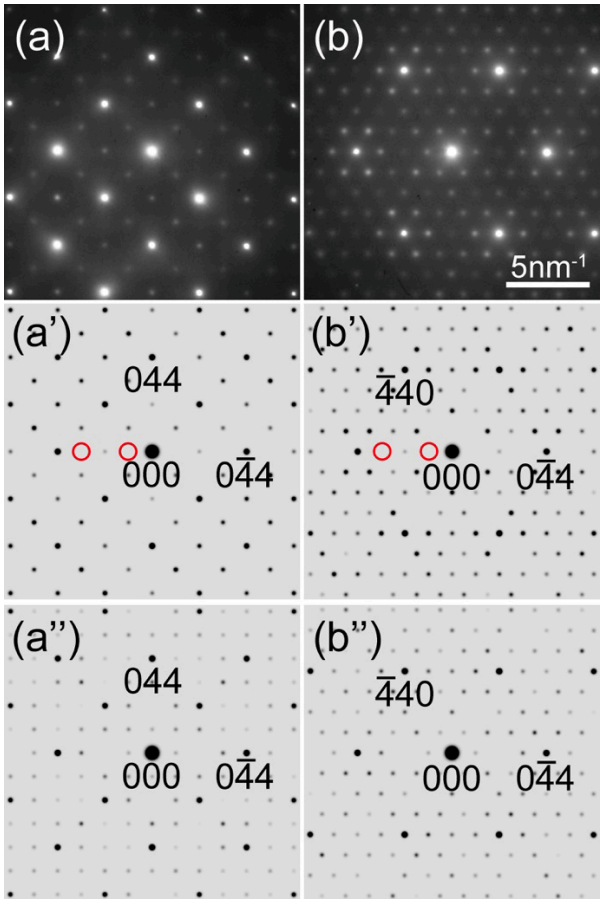
(a)
(b)
5nm-1
(a')
044
000
0$\bar{4}$4
(b')
$\bar{4}$40
000
0$\bar{4}$4
(a'')
044
000
0$\bar{4}$4
(b'')
$\bar{4}$40
000
0$\bar{4}$4

FIG. 6

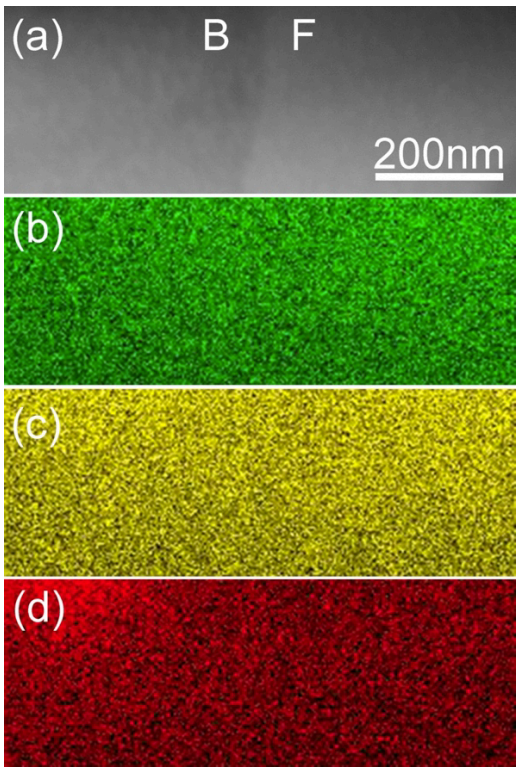

FIG. 7